










RESEARCH ARTICLE

10.1029/2022JA030861

Determining the Origin of Tidal Oscillations in the Ionospheric Transition Region With EISCAT Radar and Global Simulation Data

F. Günzkofer¹ , D. Pokhotelov¹ , G. Stober², H. Liu³ , H.-L. Liu⁴ , N. J. Mitchell^{5,6} , A. Tjulin⁷ , and C. Borries¹ 

¹Institute for Solar-Terrestrial Physics, German Aerospace Center (DLR), Neustrelitz, Germany, ²Institute of Applied Physics & Oeschger Center for Climate Change Research, Microwave Physics, University of Bern, Bern, Switzerland, ³Department of Earth and Planetary Science, Kyushu University, Fukuoka, Japan, ⁴High Altitude Observatory, National Center for Atmospheric Research, Boulder, CO, USA, ⁵British Antarctic Survey, Cambridge, UK, ⁶Department of Electronic & Electrical Engineering, University of Bath, Bath, UK, ⁷EISCAT Scientific Association, Kiruna, Sweden

Key Points:

- Twenty-day long EISCAT radar campaign shows a complex mixture of semidiurnal and diurnal tidal oscillations
- Three global circulation models show similar tidal structuring and allow to determine the influence of different forcing mechanisms
- Adaptive spectral filtering (ASF) technique allows robust fitting of tidal amplitudes and phases

Correspondence to:

F. Günzkofer,
florian.guenzkofer@dlr.de

Citation:

Günzkofer, F., Pokhotelov, D., Stober, G., Liu, H., Liu, H.-L., Mitchell, N. J., et al. (2022). Determining the origin of tidal oscillations in the ionospheric transition region with EISCAT radar and global simulation data. *Journal of Geophysical Research: Space Physics*, 127, e2022JA030861. <https://doi.org/10.1029/2022JA030861>

Received 18 JUL 2022
Accepted 15 SEP 2022

Abstract At high-latitudes, diurnal and semidiurnal variations of temperature and neutral wind velocity can originate both in the lower atmosphere (UV or infrared absorption) and in the thermosphere-ionosphere (ion convection, EUV absorption). Determining the relative impact of different forcing mechanisms gives insight to the vertical coupling in the ionosphere. We analyze measurements from the incoherent scatter radar (ISR) facility operated by the EISCAT Scientific Association. They are complemented by meteor radar data and compared to global circulation models. The amplitudes and phases of tidal oscillations are determined by an adaptive spectral filter (ASF). Measurements indicate the existence of strong semidiurnal oscillations in a two-band structure at altitudes $\lesssim 110$ and $\gtrsim 130$ km, respectively. Analysis of several model runs with different input settings suggest the upper band to be forced in situ while the lower band corresponds to upward-propagating tides from the lower atmosphere. This indicates the existence of an unexpectedly strong, in situ forcing mechanism for semidiurnal oscillations in the high-latitude thermosphere. It is shown that the actual transition of tides in the altitude region between 90 and 150 km is more complex than described so far.

Plain Language Summary Solar and atmospheric variability influence the ionosphere, causing critical impacts on satellite and ground-based infrastructure. Determining the dominant forcing mechanisms for ionosphere variability is important for prediction and mitigation of these threats. However, this is a challenging task due to the complexity of solar-terrestrial coupling processes. Tidal oscillations (mostly 12 and 24-hr periods) allow for a rough estimations of whether forcing from “above” or “below” dominates. The classical understanding is that 12-hr oscillations propagate upwards from below while 24-hr oscillations are forced at high altitudes. We analyze data from two radar systems and three global ionosphere models and show that the altitude structure of tidal oscillations is in fact more complex than classically assumed.

1. Introduction

The ionospheric dynamo region marks the transition from a collision-dominated plasma below approximately 90 km to a nearly collisionless plasma above approximately 150 km. Across this transition region, ion/electron gyrofrequencies Ω_{ie} are of the same order as collision frequencies $\nu_{in/en}$. Therefore, Pedersen and Hall conductivities maximize at these altitudes. Pedersen and Hall currents perpendicular to the magnetic field close the global magnetospheric field-aligned current system. Dynamic processes in the transition region can be forced either from “above” (plasma convection, in situ absorption of solar irradiance, auroral precipitation, etc.) or from “below” (upward-propagating waves from the lower atmosphere). Determining the actual forcing of specific effects in the transition region will help understanding the complex solar-terrestrial coupling processes.

One parameter to quantify the respective impact of atmospheric and solar effects are tidal neutral wind oscillations. The largest amplitudes can be expected for diurnal (24 hr period) and semidiurnal (12 hr period) variations. Upward-propagating atmospheric tides of both periods are mostly forced due to UV absorption by stratospheric ozone and infrared absorption by tropospheric water vapor. The classical tidal theory (Andrews et al., 1987; Lindzen, 1979; Oberheide et al., 2011) suggests the semidiurnal atmospheric tides to dominate at latitudes above approximately 45°. However, predominantly diurnal wind oscillation forced by EUV absorption at high altitudes

©2022. The Authors.

This is an open access article under the terms of the [Creative Commons Attribution License](https://creativecommons.org/licenses/by/4.0/), which permits use, distribution and reproduction in any medium, provided the original work is properly cited.

are expected to increase at high-latitudes (Straus et al., 1975). In the same region, the reconnection between the Earth's magnetic field and the interplanetary magnetic field leads to a large-scale plasma convection pattern (see e.g., Kelly, 2009). From the frame of reference of a local observer, this is perceived as 24-hr oscillation of ion velocities. This motion is transferred to the neutral particles via ion drag and frictional heating. It is classically assumed that there is a transition from dominant 12 hr to dominant 24 hr oscillation regimes at approximately 110–120 km altitude (Andrews et al., 1987) which has also been observed (Nozawa et al., 2010). However, there has been evidence for nonnegligible semidiurnal oscillations as far up as approximately 250 km (Lee et al., 2018; Schunk & Nagy, 2009; Wu et al., 2017). Whether these 12 hr oscillations are forced by atmospheric tides propagating up into the F-region or in situ generated oscillations remained an open question. One problem here is a general lack of continuous measurements in the region from 120 to 250 km.

We employ two well-established observation techniques to measure neutral wind velocities across the mesosphere-lower-thermosphere region: meteor radars and incoherent scatter radar (ISR). While meteor radars are restricted in altitude coverage by meteor trail occurrence, ISR can in principle cover the whole range from the mesopause well into the thermosphere. The actual altitude coverage, however, depends on the experiment mode and can therefore be limited. In this paper, we leverage the co-located Nordic Meteor Radar Network to validate the EISCAT neutral wind measurements. Based on the combined neutral wind data set, we estimated 12 and 24 hr oscillations at altitudes between 80 and 142 km. It has to be considered that local measurements do not provide information on the zonal wave number to separate migrating (sun-synchronous) and nonmigrating modes. We analyze data from three global ionosphere models (GAIA, WACCM-X, and TIE-GCM) to overcome the limitations of measurements in latitude, longitude, and altitude. This allows to analyze global tidal modes and the variation of amplitudes with latitude. Additionally, it can be investigated how well the amplitude variation over the limited measurement range fits the general structure. Model runs with different geomagnetic, solar, and atmospheric input can be leveraged to compare the impact of the most important forcing mechanisms. Oscillation amplitudes are extracted by applying an adaptive spectral filter (ASF) technique (Stober et al., 2017).

The further structure of the paper is as follows. Section 2 presents the experimental setup and outlines the respective methods of neutral wind measurements and amplitude fitting. The ionosphere models and the specifics of the analyzed runs are briefly introduced in Section 3. Section 4 presents the results from the analysis of measurement data and highlights the most important findings. The analysis and findings from model data are shown in Section 5. Section 6 summarizes the results from both observation and model data analyses and the paper is concluded in Section 7.

2. Instruments and Methods

2.1. EISCAT Ultra High Frequency Incoherent Scatter Radar

The EISCAT ultra high frequency (UHF) radar at Tromsø (69.6°N, 19.2°E) (Folkestad et al., 1983) is a powerful ISR with about 1.5–2 MW peak power on transmission operating at a frequency of 930 MHz. The system employs a dish with 32 m in diameter resulting in a beam width of about 0.7° corresponding to an antenna directive gain of approximately 48.1 dBi.

In this paper, we analyze UHF EISCAT observations collected during a campaign over more than 20 days in September 2005. This data set presents one of the longest continuous ISR measurements ever performed worldwide. More details on the experiment, data gaps, and data quality throughout the campaign are presented in Nozawa et al. (2010). Here, we make use of the existing data base. The EISCAT UHF radar in Tromsø was operated in the beam swinging mode in which the radar rotates back and forth between four different pointing directions (south, south-east, field aligned, and vertical) (Collis, 1995). The dwell times at the four positions and the rotation times in between result in a total time resolution of approximately 6 min. From the line of sight ion velocities measured at each pointing direction, three dimensional ion velocity vectors can be derived by inverting the radial wind equation (Nygrén et al., 2011). The advantage of beam swinging measurements is that it does not require rotating the dishes of remote receiving sites to obtain vector velocities for several altitudes. However, beam swinging measurement are limited to E-region altitudes, where the four beams have not yet dispersed too far. Three-dimensional ion velocity vectors are calculated for seven altitude gates between 96 and 142 km. An additional gate was obtained with the remote receivers at Kiruna and Sodankylä which were pointed with a fixed elevation to intersect the vertical beam at approximately 300 km altitude. The ion velocity uncertainties originate from the incoherent scatter spectrum fit uncertainties propagated through the geometrical transformation.

2.2. Neutral Wind Calculation From ISR Measurements

The procedure of calculating E-region neutral wind velocities \mathbf{u} from incoherent scatter measurements was described in Brekke et al. (1973). It assumes a steady ion velocity \mathbf{v}_i due to an equilibrium of Lorentz and ion-neutral friction force. For sufficient altitude resolution, the direct solution of the steady state ion mobility equation can be applied (Rino et al., 1977)

$$\mathbf{u} = \mathbf{v}_i - \frac{\Omega_i}{B\nu_{in}} (\mathbf{E} + \mathbf{v}_i \times \mathbf{B}). \quad (1)$$

Equation 1 requires knowledge of the magnetic field \mathbf{B} , the ion gyrofrequency Ω_i , the ion-neutral collision frequency ν_{in} , and the electric field \mathbf{E} . As magnetic field, the international geomagnetic reference field (IGRF) (Barraclough, 1988) is employed. The ion gyrofrequency is calculated from the magnetic field strength and the mean ion mass $m_i = 30.5$ amu. The electric field can be calculated at F-region altitudes and assumed to be the same (geometrical effects aside) in the E-region (Brekke et al., 1973; Nozawa & Brekke, 1999; Nozawa et al., 2010). Since ion-neutral collisions can be neglected at higher altitudes, the F-region ion velocity $\mathbf{v}_{i,F}$ is determined by $E \times B$ -drifts. The electric field is then calculated as $\mathbf{E} = -(\mathbf{v}_{i,F} \times \mathbf{B})$ where $\mathbf{v}_{i,F}$ is obtained from the highest altitude channel at approximately 300 km. The atmospheric forcing from below strongly depends on the altitude dependent ion-neutral collision frequency ν_{in} . Commonly, collision frequencies are inferred from a model neutral atmosphere (e.g., MSIS Hedin, 1991) and a collision model which can be either empirical (Chapman, 1956) or analytical (Schunk & Walker, 1973). In this paper, we apply the NRLMSISE-00 model (Picone et al., 2002) and the empirical model for ion-neutral collision frequencies

$$\nu_{in} = 2.6 \cdot 10^{-9} \cdot n_n [\text{cm}^{-3}] \cdot A^{-1/2} [\text{s}^{-1}] \quad (2)$$

described in Chapman (1956); Kelly (2009), with neutral particle density n_n and $A = m_i$ [amu]. However, the accuracy of any collision model at altitudes ≥ 120 km has to be considered carefully (Nozawa et al., 2010; Williams & Virdi, 1989). A direct measurement of the ion-neutral collision frequencies would be possible with the current EISCAT system due to its multifrequency capability with simultaneous operation of UHF and VHF radars (Grassmann, 1993; Nicolls et al., 2014). However, there were no multifrequency experiments scheduled during the investigated campaign. This could provide an option for further improvement in future investigations.

2.3. Meteor Radar

Since the derivation of neutral wind velocities from EISCAT measurements is not as well established, meteor radar measurements can be used as a reference at the lower boundary. In this paper, measurements from EISCAT and the Kiruna meteor radar will be merged to test the validity of the procedure described in the previous section. As an additional advantage, the total observed altitude range is extended significantly downwards.

Meteor radars have become a ubiquitous sensor capable of monitoring winds in the mesosphere and lower thermosphere. These instruments observe small meteoroids, which are formed when extraterrestrial particles with a sufficient kinetic energy enter the Earth's atmosphere. Small meteoroids can penetrate deep into the atmosphere until they encounter a sufficiently dense region. The impinging atmospheric molecules and atoms decelerate and heat the particles to such an extent that the meteoric material is vaporized and atoms are released from the meteoroid. Due to the collisions with the ambient neutral atmosphere the released atoms are thermalized and form an ambipolar diffusing plasma trail, often called a meteor trail. This trail provides a coherent scatter target and allows to measure wind velocities since it drifts with the neutral winds. Specular meteor radars detect most of these trails at altitudes between 70 and 110 km. For a large enough number of meteor trails, horizontal wind velocities can be measured with an "all-sky"-fit (Hocking et al., 2001). This is usually done with a time resolution of 1 hr and 2 km altitude bins.

In Kiruna (67.9°N, 21.1°E), a meteor radar has been continuously operated since 1999 and therefore provides measurement for the time of the EISCAT campaign described above. Meteor radars have been used for the investigation of various types of waves in the upper atmosphere, including atmospheric tides, and provide a well-tested measurement method (Pokhotelov et al., 2018; Stober et al., 2021).

2.4. Adaptive Spectral Filtering

The determination of tidal amplitudes and phases is done using the adaptive spectral filtering (ASF) technique (Stober et al., 2017). Thereby, the neutral wind data in zonal and meridional direction is separately fitted for a mean background wind and several periodic components. We apply two separate filters on measurement and model data. A local ASF is used to fit for 24, 12, and 8 hr oscillations in a combined neutral wind data set from ISR and meteor radar measurements. A global ASF is applied on model data which allows to obtain zonal wavenumbers additionally to oscillation periods. The nomenclature of global tidal modes gives information on period (D: diurnal, S: semidiurnal), propagation direction (W: westward, E: eastward) as seen from an observer at a fixed geographic location on Earth and the zonal wavenumber k (Smith, 2012). While in principle the latter can take any integer value, we will restrict our analysis to $0 \leq k \leq 3$ since the by far largest amplitudes are expected for the two sun-synchronous, migrating tidal modes DW1 and SW2 (Smith, 2012). Unless otherwise stated, amplitudes in this paper have been averaged over a sliding window of 1 day length. The ASF has shown to be a robust frequency analysis method for unequally spaced data (spatially and temporal). The technique is also reliable for higher relative uncertainties of the fitted data since it takes these uncertainties into account. Due to the fitting of phases, the propagation of nonstationary processes (phase drifts over time) can be estimated similar to holographic analysis (Stober et al., 2020). The robustness of the fitting for short-time windows enables a good resolution of the day-to-day variability of amplitudes compared to other methods. The ASF has been successfully extended and applied to fit for global tidal modes (Baumgarten & Stober, 2019; Stober et al., 2020).

3. Models

3.1. Ground-To-Topside Model of Atmosphere and Ionosphere for Aeronomy

The Ground-to-Topside Model of Atmosphere and Ionosphere for Aeronomy (GAIA) is a global circulation model (GCM) giving neutral dynamics for all altitudes from the ground up to approximately 600 km (Jin et al., 2012). GAIA data has been compared and verified with experiment data from numerous different apparatuses for time spans up to several decades. The GAIA data set used for the analysis presented in Section 5 has been previously applied for long-term investigations in H. Liu et al. (2017) and Stober et al. (2021). We summarize the most important features and refer to these publications for more detailed information.

The atmosphere up to approximately 30 km altitude is constrained to the JRA-25/55 reanalysis (Kobayashi et al., 2015) using a nudging technique. The measurements used in the reanalysis are listed in Onogi et al. (2007). While the solar irradiance, and thereby EUV absorption, is parametrized with the F10.7 index, the geomagnetic activity is set to a constant value. Therefore, the cross polar potential is held at 30 kV for all model data, corresponding to a moderate level of geomagnetic activity. The neutral wind components are provided on a grid with a resolution of 1° in latitude and 2.5° in longitude. The altitude resolution is $1/5$ of the respective scale height at each altitude. The analysis presented in this paper has been conducted with preprocessed files giving the data in 10 km altitude bins. The time resolution is 0.5 hr.

3.2. Whole Atmosphere Community Climate Model Extension (SD)

The Community Earth System Model is a combination of models covering different parts of the Earth system (Hurrell et al., 2013). The Whole Atmosphere Community Climate Model Extension WACCM-X (H.-L. Liu et al., 2018) is the part of the CESM describing the atmosphere from the ground up to ≥ 500 km. The data presented in this paper was generated with a Special Dynamics run WACCM-X(SD) (Gasparini et al., 2020) and previously used in Stober et al. (2021). Again, we only give a brief overview and refer to the mentioned publications.

The lower atmosphere is constrained up to approximately 50 km to NASA's reanalysis MERRA (Gelaro et al., 2017; Rienecker et al., 2011). Other than the analyzed GAIA run, WACCM-X(SD) does not set a fixed cross polar potential. The polar convection is calculated using the *Heelis* model (Heelis et al., 1982) and the geomagnetic activity is therefore parametrized by the Kp index. As proxy for EUV absorption, WACCM-X also utilizes the F10.7 index. The longitudinal resolution is 2.5° and values are given in 3 hr intervals. Since the model is evaluated on hydrostatic pressure levels, the altitude range extends from 992.5 hPa near the ground up to approximately $4 \cdot 10^{-10}$ hPa. The height resolution above approximately 50 km is $1/4$ of the respective scale height. The corresponding geopotential altitudes are given for each time and position and extend roughly from the ground up to approximately 500 km. In the transition region, the geopotential height resolution varies between 1

and 5 km. The different parametrization of geomagnetic activity in the analyzed GAIA and WACCM-X runs are ideal to investigate its influence on neutral winds at different altitudes. However, since both models extend to the ground and are restrained to reanalysis of meteorological data (Stober et al., 2021), it is not feasible to separate the impacts of atmospheric forcing in these models.

3.3. Thermosphere Ionosphere Electrodynamic General Circulation Model

The Thermosphere Ionosphere Electrodynamic General Circulation Model (TIE-GCM) (Richmond et al., 1992) is a standalone ionosphere model and also part of the Coupled Magnetosphere-Ionosphere-Thermosphere Model (Qian et al., 2014). The data presented in this paper was generated from several runs performed with the TIE-GCM Model Version 2.0.

In contrast to the two models described above, TIE-GCM does not extend down to the ground, but applies a lower boundary condition at approximately 99 km altitude. The horizontal neutral winds and neutral temperatures at the boundary are specified by input files. These quantities include the monthly averaged amplitudes and phases of diurnal and semidiurnal tides which are by default given by the Global Scale Wave Model (GSWM) (Hagan & Forbes, 2002, 2003). For the present paper, the GSWM boundary data has been modified to give the tidal measurements from the Kiruna meteor radar for the investigated time. Performing separate runs with empirical tidal input and with zero tidal input allows to assess the impact of atmospheric dynamics and the forcing from below. Same as for WACCM-X, the *Heelis* model is applied to obtain the cross polar potentials and geomagnetic activity is parametrized according to the Heelis parametrization (Heelis et al., 1982). While per default solar irradiance is parametrized by the F10.7 index, we conduct an additional run with a fixed F10.7 index of 70 to identify the impact of EUV absorption. TIE-GCM gives output data on a $2.5^\circ \times 2.5^\circ$ grid with a time resolution of 1 hr. Furthermore, TIE-GCM data is provided on logarithmic altitude coordinates (atmospheric ln pressure coordinate) $\ln\left(\frac{p_0}{p}\right)$ for the pressure p at a certain altitude. The reference pressure $p_0 = 5 \cdot 10^{-5}$ hPa corresponds roughly to approximately 225 km altitude and the atmospheric ln pressure coordinate ranges from -6.875 to 7.125 in 0.25 increments. This corresponds to a resolution of $1/4$ in scale height units. The geopotential altitude ranges from approximately 96 to 590 km with a resolution that steadily increases from approximately 2 to 18 km with increasing height.

4. Experiment Data

This section will give an overview on the results from analysis of experimental data obtained with the instruments presented in Section 2.

4.1. Neutral Wind

As described in Section 2.1, the four line of sight ion velocities measured were geometrically transformed to a geographic reference frame. From those, the steady state ion equation was applied to obtain neutral wind vectors. Figure 1 shows the calculated neutral winds in zonal and meridional directions for the measurement channel at 115 km altitude.

Error bars shown in Figure 1 are calculated from the ion velocity measurement uncertainties by propagation of uncertainty through the whole procedure described in Section 2.2. Uncertainties of the ion-neutral collision frequency, which can have a major impact (Williams & Virdi, 1989), are not shown. While the relative uncertainties at altitudes ≥ 110 km are reasonably small ($\leq 40\%$), they tend to increase with decreasing altitudes ($\leq 70\%$). The lower electron density results in smaller signal-to-noise ratios and consequently leads to increased statistical uncertainties in the derived incoherent scatter spectrum parameters. Neutral wind velocities calculated from EISCAT measurements at low altitudes should therefore be treated carefully when looking at absolute values. The determination of tidal oscillation amplitudes is still possible with reasonable accuracy due to the robustness of the ASF technique (see Section 2.4). The strong outliers at single timepoints (around day 19) and data gaps (around day 21) visible in Figure 1 are most likely caused by problems with the radar system and can also be handled by the ASF method.

The diurnal and semidiurnal amplitudes are determined separately for each altitude level. Figure 2 shows the amplitudes of tidal oscillations measured by the Kiruna meteor radar ($80 \text{ km} \leq h \leq 104 \text{ km}$) and the EISCAT UHF in Tromsø ($96 \text{ km} \leq h \leq 142 \text{ km}$). To see possible correlations, indices for geomagnetic activity and solar

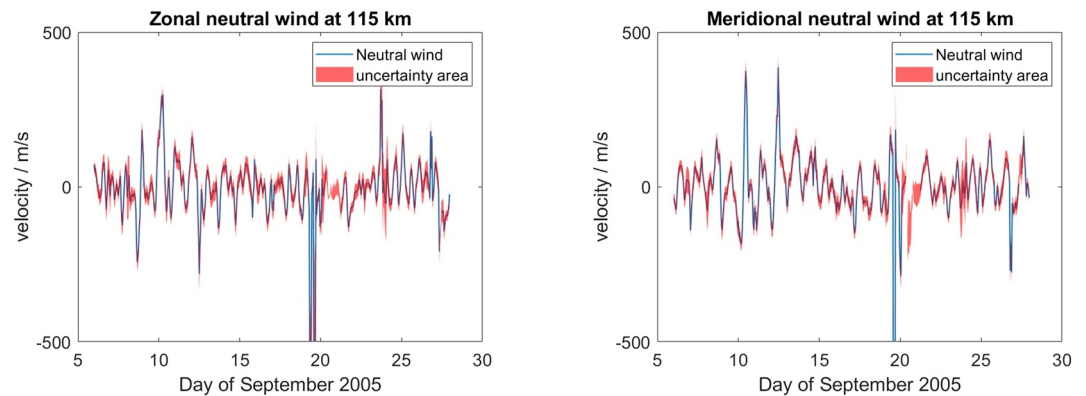


Figure 1. Neutral winds at 115 km altitude in zonal (left) and meridional (right) direction measured with the EISCAT radar. The uncertainty has been determined from the measurement uncertainty by means of Gaussian error propagation.

irradiance during the time of the measurement campaign are also shown in Figure 2. The geomagnetic activity is quantified by the Kp index since it is often used to parametrize polar plasma convection. The F10.7 index is used to quantify solar activity and EUV absorption.

Figure 2 shows the merged amplitudes of both systems and includes the transition altitude between both instruments at about 100 km. Additionally, the graphic indicates the presence of a data gap around September 21st for the EISCAT observations, whereas the meteor radar wind time series remains uninterrupted during the entire period. To compare the measurements in the overlap region, the wind velocities caused by tidal oscillations are calculated from the fitted amplitudes and phases. The tidal winds averaged across the coverage overlap of both instruments show moderate correlation ($R = 0.54$). It should be noted that the overlap is at the edge of cover-

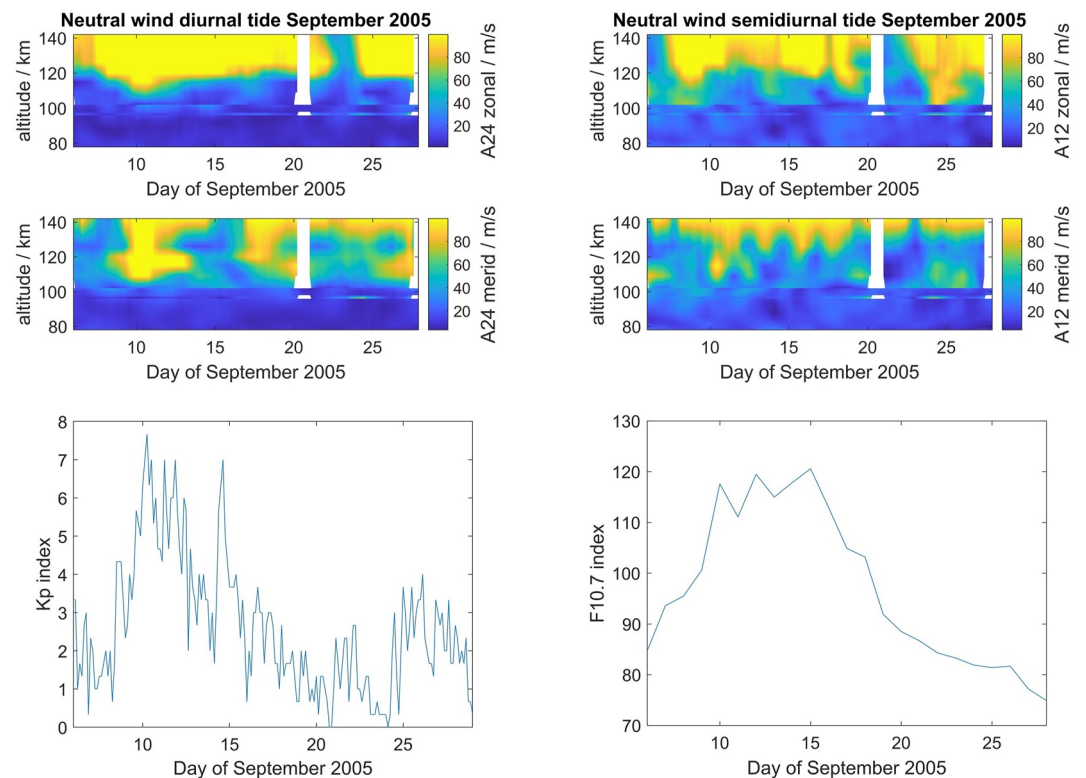


Figure 2. Top: the amplitudes of diurnal (left) and semidiurnal (right) oscillations in zonal (top) and meridional (bottom) direction during September 2005. Data from EISCAT and meteor radar are merged together. Bottom: the geomagnetic activity (Kp index, left) and the solar irradiance (F10.7 index, right) during the measurement time.

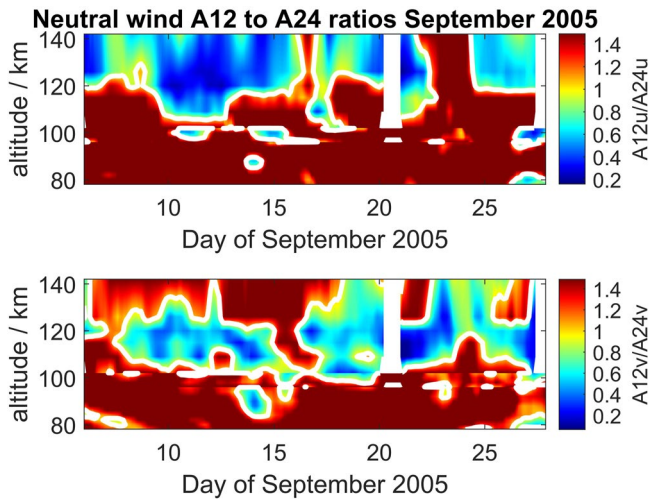


Figure 3. Ratio of semidiurnal to diurnal amplitudes in zonal (top) and meridional (bottom) neutral winds. The meridional component shows a two-band structure of dominant semidiurnal oscillations.

age of both systems where the respective uncertainties are increased. Therefore deviations of ISR and meteor radar measurements have to be expected. Considering these mitigating circumstances, the EISCAT neutral winds calculated with the procedure from Section 2.2 are validated.

While the amplitudes of both tidal modes generally increase with altitude, it can be seen that there are differences regarding altitudinal structure and time variability.

The next step is the determination of the dominant tidal mode at each time and altitude. Therefore, the amplitude ratio of semidiurnal to diurnal oscillations is calculated and shown in Figure 3.

The ratio of zonal amplitudes A_{12u}/A_{24u} in the upper plot of Figure 3 corresponds very much to what is expected from the classical tidal picture (Lindzen, 1979). Semidiurnal variations are predominant up to altitudes of approximately 110–120 km. Above that, diurnal oscillations have larger amplitudes most of the time. Meridional tidal amplitudes, on the other hand, show a distinctly different altitude structure. While the transition from predominant semidiurnal to diurnal tide also takes place at and around 110 km altitude, there is an upper band of strong semidiurnal oscillations especially during the first half of September. This apparent weakening of the upper 12 hr

band around equinox is an important feature since atmospherically forced semidiurnal tides have been shown to undergo such an autumn transition (Pedatella et al., 2021). Whether this upper band is generated in situ or forced by some atmospheric tidal mode that propagates unusually far up remains to be investigated in more detail.

4.2. Phase Progression Analysis

As described, the ASF technique also allows to extract the phase of tidal oscillations which can be used to distinguish propagating and evanescent tidal modes. The time of maximum should be steadily shifted with altitude for an upward-propagating oscillation, showing as a swift change of phase. An evanescent tidal mode would result in a constant phase with altitude. A rapid transition from steadily shifted to constant phase would therefore suggest a transition of forcing mechanism. However, the phase of a propagating mode also asymptotes toward a constant value at higher altitudes which makes the distinction nontrivial. Figure 4 shows the phase of diurnal and semidiurnal oscillations obtained from ASF analysis of the combined EISCAT and meteor radar data set. Altitude profiles of the semidiurnal tide phases at an example time are shown as well.

The phases of diurnal and semidiurnal oscillations in Figure 4 show a complex mixing of tidal modes, since migrating and nonmigrating modes cannot be distinguished from local measurements. However, while there is a lot of dynamics in the tidal phases throughout the month, the classically expected structure can be seen when looking at the median over the entire measurement time. The median altitude profiles of semidiurnal phases in the zonal and meridional wind are shown in the bottom left corner of Figure 4. The phases show a steady shift in the time of maximum up to altitudes of approximately 110–120 km. Above that, the phase progression seems to stop or even reverse. This transition can be seen more clearly at specifically chosen timepoints, one of which is shown in the bottom right corner of Figure 4. The transition to a nearly constant phase seems to happen rapidly, especially in the meridional winds, indicating a transition from propagating to in situ tidal modes. However, due to the aforementioned asymptoting of the phases of propagating tidal modes, in situ generation of the high altitude semidiurnal oscillations cannot be conclusively confirmed from the altitude-phase plot alone.

4.3. High Altitude ion Velocities

E-region neutral winds are inferred from the ion velocity observations of EISCAT. The ion velocities at approximately 300 km altitude allow to estimate the convection electric field required in Equation 1. If 12 hr oscillations of the neutral wind are forced by plasma convection at high altitudes, ion velocities at 300 km altitude should also exhibit significant semidiurnal amplitudes. Diurnal and semidiurnal amplitudes are determined by the same ASF applied on the neutral wind data and shown in Figure 5.

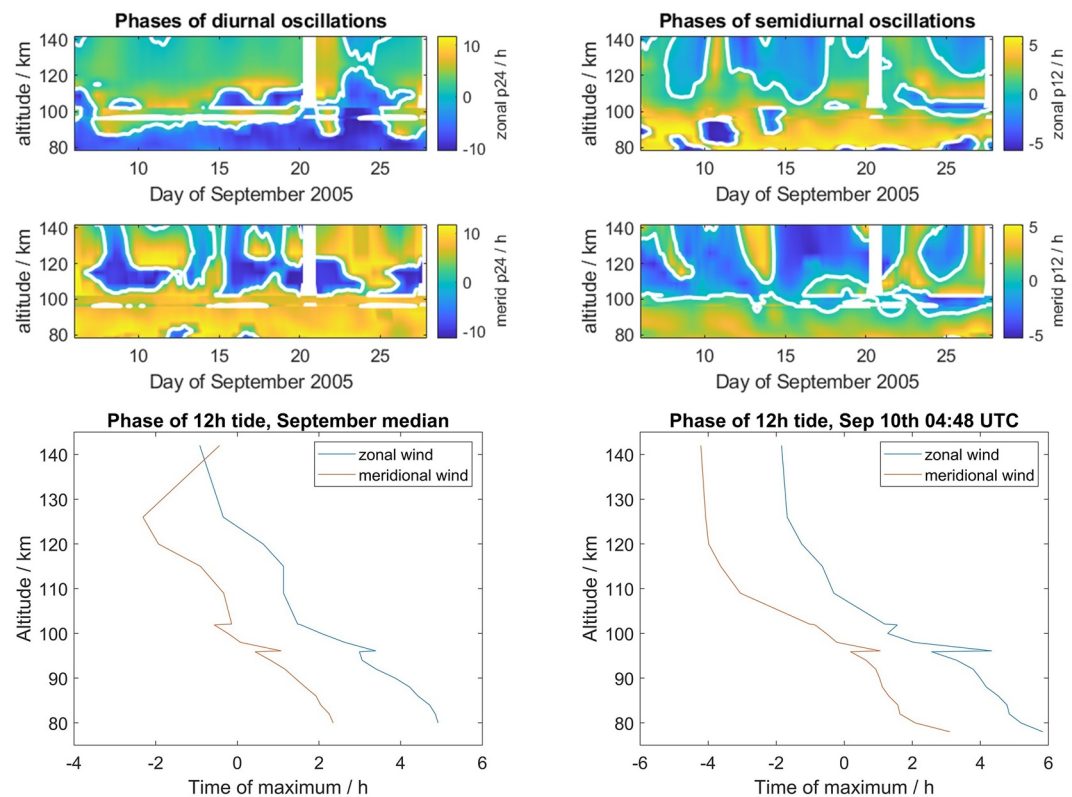


Figure 4. Top: phases of diurnal and semidiurnal oscillations obtained from a combined EISCAT and meteor radar neutral wind data set. Bottom: altitude profiles of 12 hr tide phases as median over the whole measurement time (left) and at an exemplary time (right).

The ion velocity oscillation amplitudes in Figure 5 show a general trend similar to the geomagnetic activity index plotted in Figure 2. The polar plasma convection is expected to be perceived as a diurnal oscillation of ion velocity by a local observer. Consequently, diurnal amplitudes are clearly larger than semidiurnal amplitudes. However, there are significant 12 hr oscillation amplitudes sometimes even exceeding 50% of the 24 hr amplitudes. A possible explanation for a perceived semidiurnal periodicity of the polar plasma convection might be an irregular shaped convection pattern.

The semidiurnal component of the polar plasma convection provides one possible interpretation for the neutral wind tidal oscillations shown in Figure 3. However, this cannot be definitely determined from the available

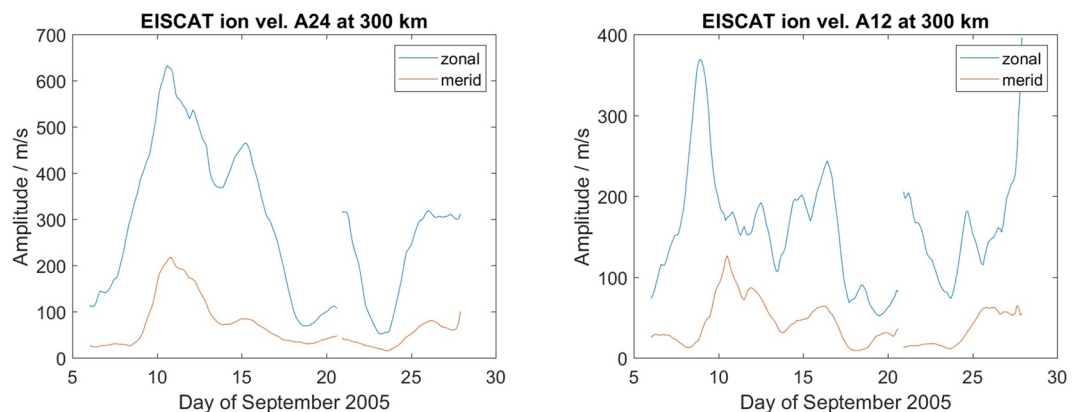


Figure 5. Diurnal (left) and semidiurnal (right) amplitudes in the ion velocities from the F-region altitude channel measured with EISCAT.

measurement data. Global ionosphere models can give additional insight in longitudinal wavenumbers of the observed tidal modes. Also, a possible variation of oscillation amplitude with latitude could be determined from model data. Such a variation would be expected in case the forcing mechanism is a high-latitude effect like polar plasma convection.

5. Model Data

This section will give an overview on the results from analysis of global simulation data with the models presented in Section 3.

5.1. Neutral Wind

GCMs provide neutral wind velocities on a global longitude and latitude grid. The model data is analyzed for the period from day 200–320 (19 July to 16 November) of the year 2005. The plots in this section are restricted to the days of the EISCAT measurement campaign to allow a direct comparison of the dynamics over these days. However, since the main interest of this work is to investigate the altitudinal structure of tidal oscillations, an altitude range from 80 to 300 km will be shown. The neutral wind velocities are analyzed at two latitudes, one of them corresponding to the measurement position in Tromsø, the other one for comparison at mid-latitudes (44°N). The GCM longitudinal resolution is 2.5° in all models.

As described in Section 1, the model data is not only fitted for the time period of neutral wind oscillations but also for zonal wave numbers $0 \leq k \leq 3$ by the ASF. The amplitudes of each tidal mode were evaluated at 20°E longitude to ensure that a comparison with the observations is meaningful. As expected, the clearly dominating tidal modes for both diurnal and semidiurnal oscillations are the sun-synchronous migrating modes DW1 and SW2. Therefore, we only present the obtained amplitudes for these modes. To investigate the impact of forcing from below, TIE-GCM runs with different lower boundaries are compared. A third TIE-GCM run with constant low solar input is conducted to show the impact of EUV absorption.

5.1.1. Impact of Geomagnetic Activity (GAIA and WACCM-X(SD))

As described in Section 3, the analyzed GAIA run applies a constant cross polar potential, corresponding to a low geomagnetic activity. The impact of geomagnetic activity will be determined by comparison to the WACCM-X(SD) run, for which plasma convection was parametrized with the Kp index. Additionally, we compare tidal amplitudes for both models at high and mid-latitudes to show the impact of high-latitude effects. Figure 6 shows the amplitudes of DW1 and SW2 oscillations obtained from GAIA and WACCM-X(SD) data evaluated at the Tromsø geographical position. To ensure comparability between data from model runs with different forcing or evaluated at different latitudes, the color scale is kept the same for all view graphs.

Semidiurnal amplitudes of zonal and meridional wind component show a pronounced maximum at or slightly above approximately 100 km altitude in both models. According to classical tidal theory, this is associated with upward-propagating atmospheric tides. The amplitude of vertically propagating tides is supposed to show an exponential growth up to the altitude at which molecular dissipation damps it, presumably somewhere between 100 and 130 km (Truskowski et al., 2014). At higher altitudes, the amplitude depends on the region and strength of in situ forcing mechanisms. At higher altitudes $\gtrsim 130$ km, there are distinct differences between the two models and also between zonal and meridional wind component. GAIA shows an upper band of strong semidiurnal amplitudes but only in the meridional and not in the zonal component. This asymmetry between zonal and meridional component agrees well with what has been detected in the EISCAT data (see Figure 3). The WACCM-X(SD) run also shows more than one region of strong 12 hr oscillations, though the altitude structure of this regions is more complicated than in the GAIA run. Also, the asymmetry between zonal and meridional component is not as pronounced as in GAIA. This might both be caused by the parametrization of geomagnetic activity and consequently different size, shape, and intensity of the plasma convection pattern. This can also be seen in the diurnal oscillation amplitudes where both models show large amplitudes in the meridional component at high altitudes. However, WACCM-X(SD) gives larger amplitudes and there are major differences between the models with regard to the zonal component.

It can be seen that both models give a complex structuring of SW2 oscillations, especially the existence of large amplitudes at high altitudes. Though there are distinct differences between both models, these might be caused

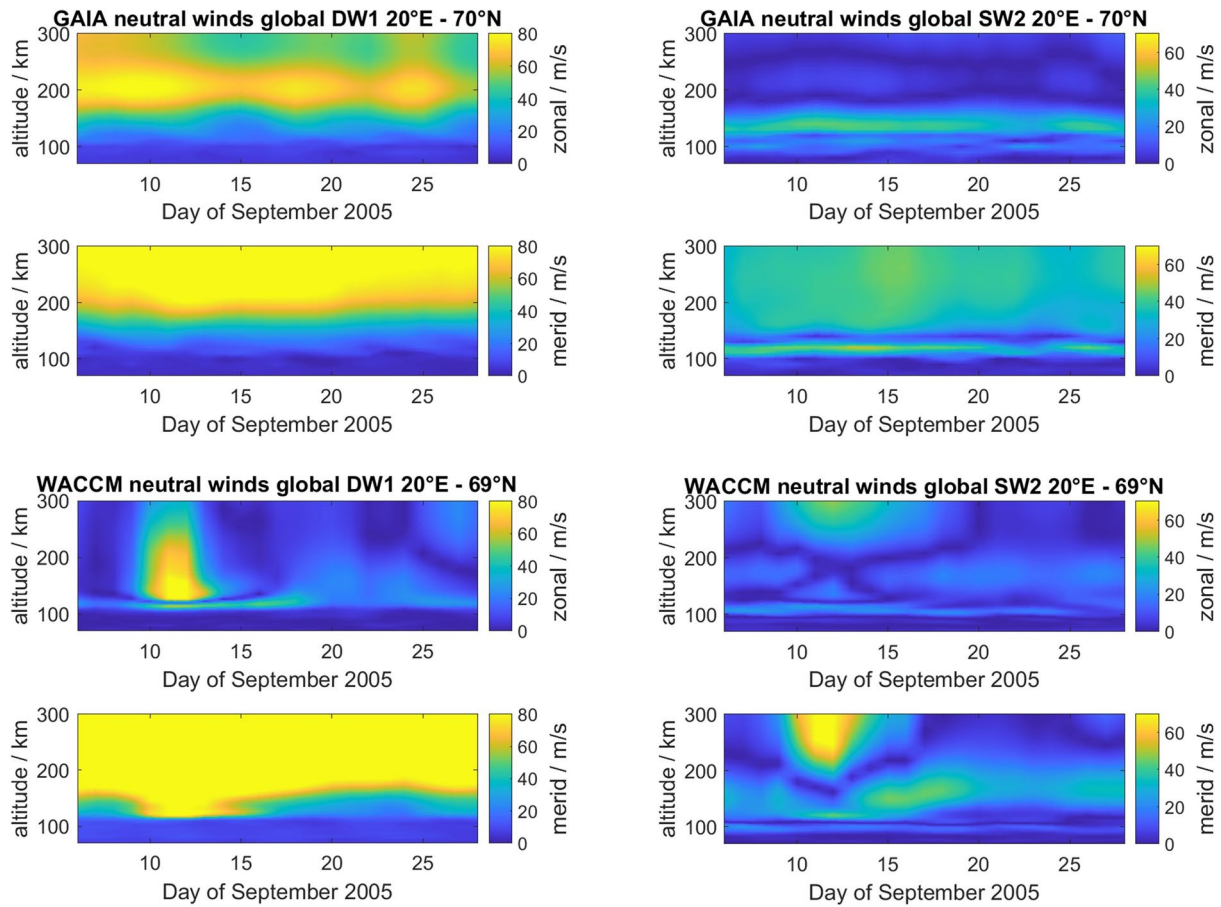


Figure 6. Comparison of GAIA (top) and WACCM-X(SD) (bottom) amplitudes of the DW1 (left) and SW2 (right) tidal modes at high-latitudes (70°N).

by the different parametrization of geomagnetic activity. A forcing of both DW1 and SW2 oscillations by polar plasma convection seems to provide a possible explanation of the observed results. However, other in situ forcing mechanisms need to be considered as well as the possibility that atmospheric tides interact with the in situ forced modes.

Polar plasma convection only impacts the high-latitude region and therefore any convection forced oscillations would not be present at mid- or low-latitudes. Evaluating model tidal amplitudes at mid-latitudes therefore allows to narrow down the possible forcing mechanisms. Figure 7 shows the amplitudes of the same tidal oscillation modes as Figure 6 but at 44°N latitude.

The diurnal amplitudes in zonal and meridional neutral winds are decreased in both models at all altitudes. There clearly is a strong high-latitude forcing mechanism of tidal oscillations at high altitudes. However, GAIA and WACCM-X(SD) show significantly different structures of diurnal oscillations.

The SW2 oscillation maximum at approximately 110 km associated with upward-propagating tides is also visible at mid-latitudes, providing confidence to our previous interpretation. The SW2 amplitudes at high altitudes, on the other hand, are significantly reduced. This suggests that there is a strong forcing mechanism of high altitude SW2 oscillations at high-latitudes. However, it also shows that there is likely not only one single forcing mechanism. The complex structuring of tidal oscillations at high altitudes is therefore presumably caused by the varying forcing strength and interference of several mechanisms. However, the main interest of this paper is to determine the mechanism causing the large amplitudes of high altitude SW2 oscillations at high-latitudes. While the strong 12 hr oscillations of EISCAT ion velocities at high altitudes as well as the asymmetry of zonal and meridional wind component seem to indicate polar plasma convection as one possible mechanism, the impact of propagating atmospheric and EUV-forced tides might be just as large.

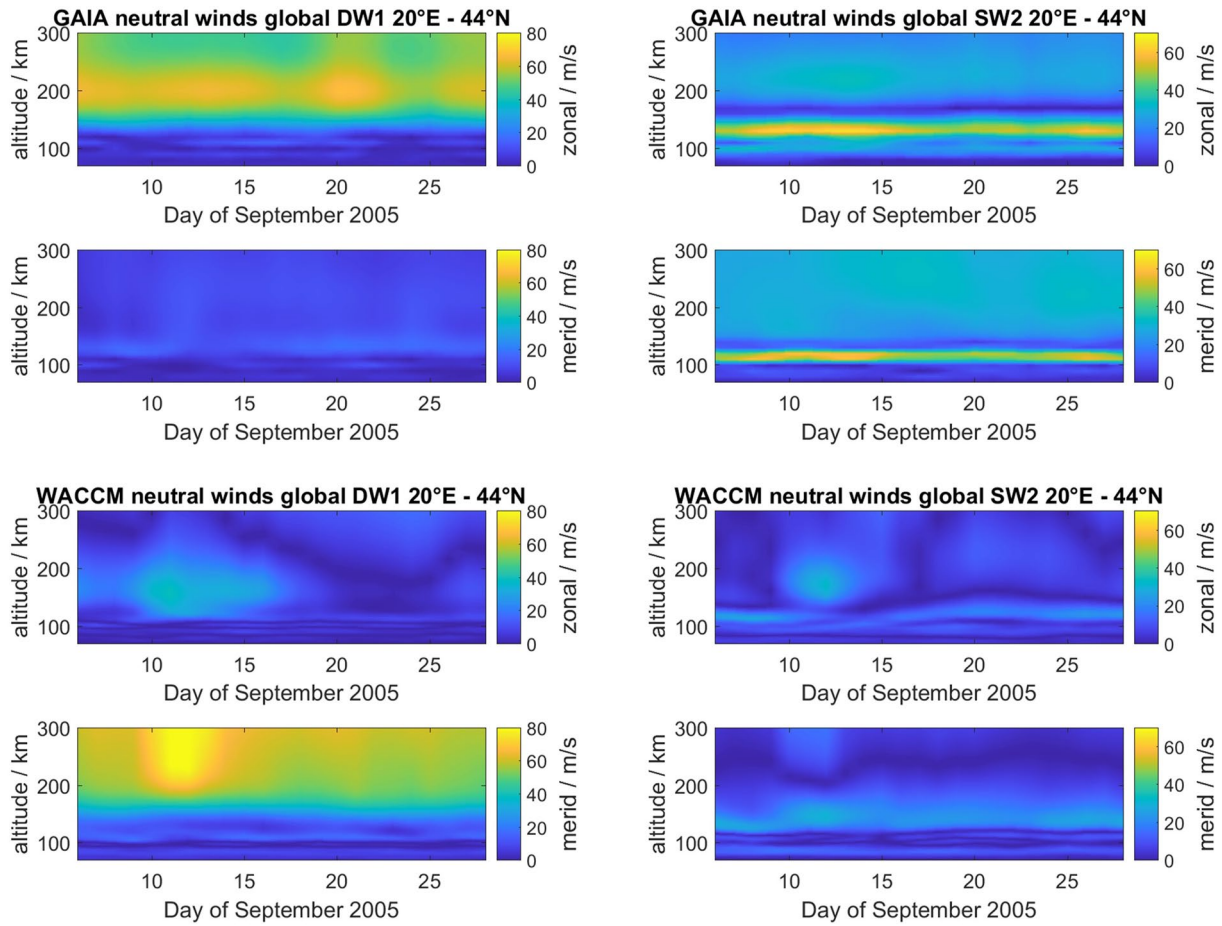


Figure 7. Comparison of GAIA (top) and WACCM-X(SD) (bottom) amplitudes of the DW1 (left) and SW2 (right) tidal modes at mid-latitudes (44°N).

5.1.2. Impact of Atmospheric Forcing (TIE-GCM)

Comprehensive models such as GAIA and WACCM-X involve complex processes, which have to be parametrized posing challenges to conduct and investigate more isolated processes. TIE-GCM offers the possibility to investigate the ionosphere and thermosphere by applying a well-defined lower boundary condition describing the middle atmospheric forcing. Figure 8 shows the results of two different model runs, one performed using an empirical input for tidal oscillations at 99 km and one with tidal amplitudes set to zero at the boundary. The dominance of sun-synchronous tidal modes is found in TIE-GCM as well and the dynamics of DW1 oscillations is similar to what has been found in the WACCM-X(SD) data. Therefore, further investigations are restricted to SW2 oscillations for the TIE-GCM model runs. As in the previous section, tidal amplitudes are evaluated at high- and mid-latitude.

At high-latitudes, the TIE-GCM run with empirical tidal forcing exhibits a similar SW2 amplitude structure as the ones shown in Figure 6 from GAIA and WACCM-X(SD). This run indicates a two band structure accompanied by a transition of the upper band around the autumn equinox. From the radar phase measurements in Figure 4 we assumed that the lower band is forced by upward-propagating tide, which is confirmed by the TIE-GCM run with zero tidal input at the boundary. In this run, shown on the right side of Figure 8, the lower band mostly vanishes, whereas the upper band appears to be not affected. This seems to exclude lower atmospheric forcing as origin of the upper SW2 band structure. At mid-latitudes, we obtain a similar picture as already found in Figure 7, showing a notably reduced SW2 amplitude at high altitudes and a nearly unaffected amplitude at lower altitudes. Most interestingly here, the high altitude SW2 oscillations seem to be partly forced by the propagating tides from the middle atmosphere since they are significantly reduced in the run with zero tidal forcing at the lower boundary. So while there clearly is strong in situ forcing of SW2 oscillations, upward-propagating atmospheric tides cannot

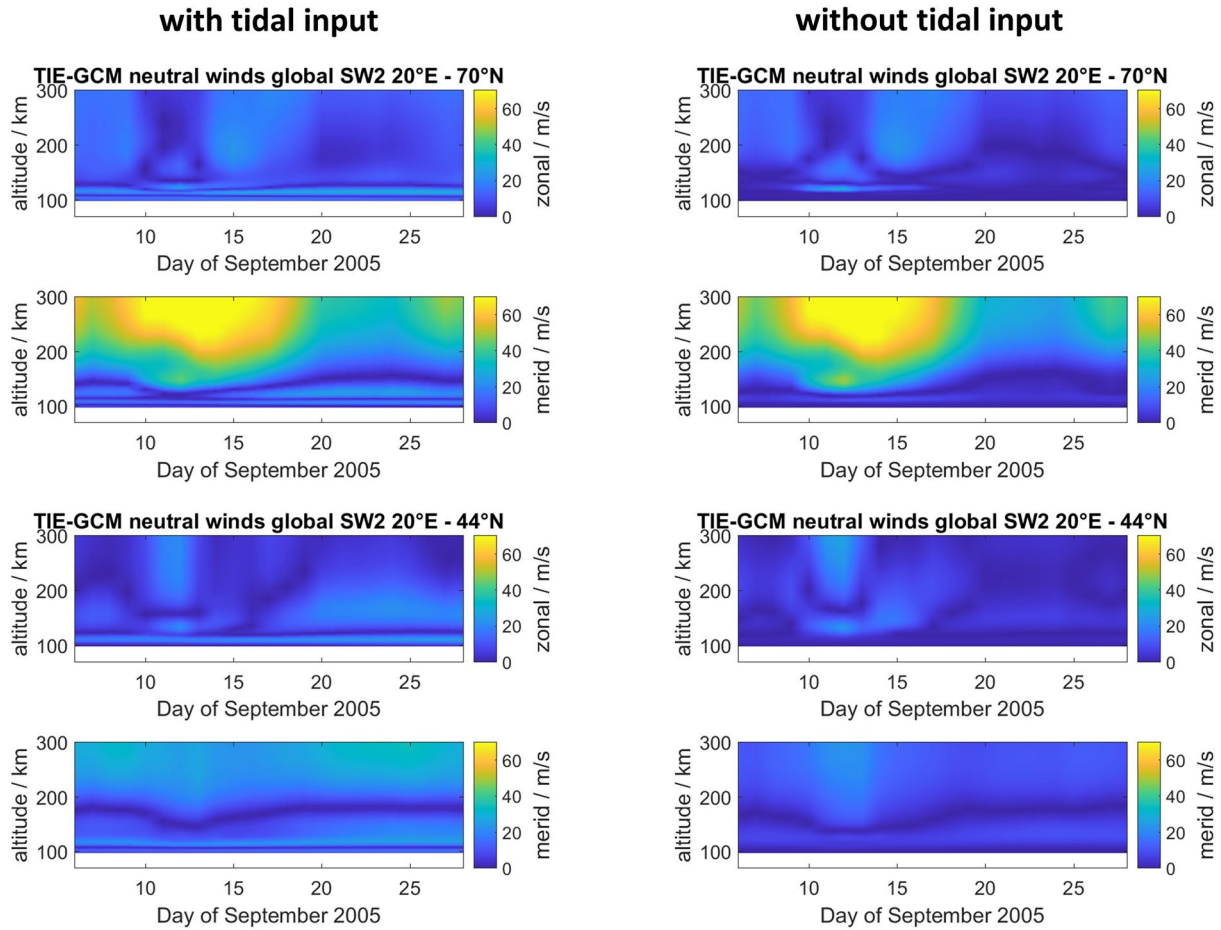


Figure 8. Amplitudes of SW2 tidal oscillation from the TIE-GCM model at high- (up) and mid-latitudes (bottom). Presented are two separate runs with imposed (left) and zero (right) atmospheric tidal input.

be completely neglected. Especially the interference of in situ and propagating modes is likely a reason for the complex structure of tidal oscillations. As for the in situ forcing mechanism, it should be noted that tidal oscillations forced by EUV absorption above the lower boundary are still present in TIE-GCM. The impact of EUV absorption is studied with an additional TIE-GCM run.

5.1.3. Impact of EUV Absorption

A TIE-GCM run with fixed daily $F_{10.7} = 70$ and 81-day-averaged $F_{10.7a} = 70$ as EUV-proxy has been conducted. In comparison with the actual $F_{10.7}$ values in Figure 2 it can be seen that this corresponds to low EUV irradiance. As tidal input at the boundary, the same settings as for the run shown on the left side of Figure 8 have been applied. Figure 9 shows the SW2 oscillation amplitudes obtained from this new run, as before evaluated at high- and mid-latitudes.

It can be seen in Figure 9 that with a fixed, low EUV irradiance, the high altitude oscillation amplitudes are significantly reduced. Especially between the 10th and 15th of September, where the actual $F_{10.7}$ index maximized (see Figure 2), there is a visible reduction of tidal amplitudes at ≥ 180 km altitude, both at high- and mid-latitudes. As expected from theory (Straus et al., 1975), the tidal amplitudes from EUV forcing seem to be larger at high-latitudes. It has to be considered that even for low $F_{10.7}$ values there still is a gradient in EUV absorption between day and night side. Therefore tidal oscillations forced by EUV absorption are still present with reduced amplitude. The extension of the upper SW2 band to altitudes $\lesssim 180$ km seems to remain the same for low EUV absorption. Also, there still is considerable dynamics of the high altitude oscillations. This makes a second in situ forcing mechanism, like polar plasma convection, a more likely explanation than the reduced and constant amplitudes due to EUV absorption gradients.

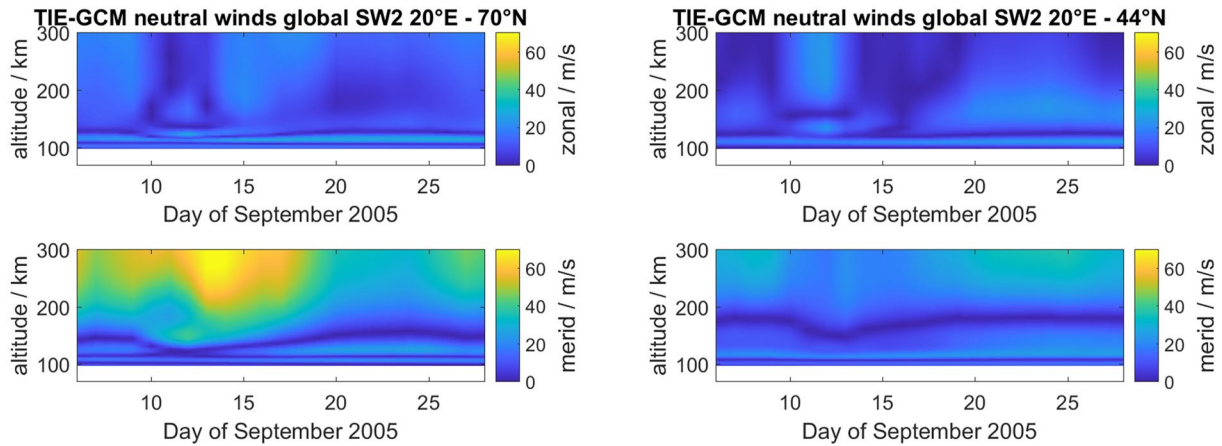


Figure 9. SW2 oscillations from a separate TIE-GCM run with fixed F10.7 and F10.7a values. Amplitudes are shown at high- (left) and mid-latitudes (right).

5.2. Phase Progression Analysis

As discussed in Section 4.2, propagating and evanescent tidal modes can be distinguished, to some extent, by means of phase progression analysis. Semidiurnal oscillations observed in EISCAT data below 120 km have been identified to correspond to upward-propagating atmospheric tides (Nozawa et al., 2010) (see also Section 4.2). To extend the altitude coverage into the F-layer at mid- and polar-latitudes, the phases of tidal oscillations in global models have been analyzed. Figure 10 shows the time of maximum of the SW2 tidal mode in the meridional winds extracted from GAIA and WACCM-X(SD) at 70°N latitude. To emphasize the autumn transition seen in the oscillation amplitudes, the whole range of model data from day 200 to day 320 is shown here. We also show the vertical phase profile of 12 hr oscillations as given by GSWM for September, where only upward-propagating and no in situ forced tides are included.

GAIA and WACCM-X(SD) show a steady phase progression at low altitudes and nearly constant phase at higher altitudes. Other than that, the SW2 phase is distinctly different in both models. However, the different forcings like gravity wave parametrization, reanalysis and cross polar potential can in principle all cause differences in phases between the two models. A nearly constant phase at high altitudes could be found for a propagating mode

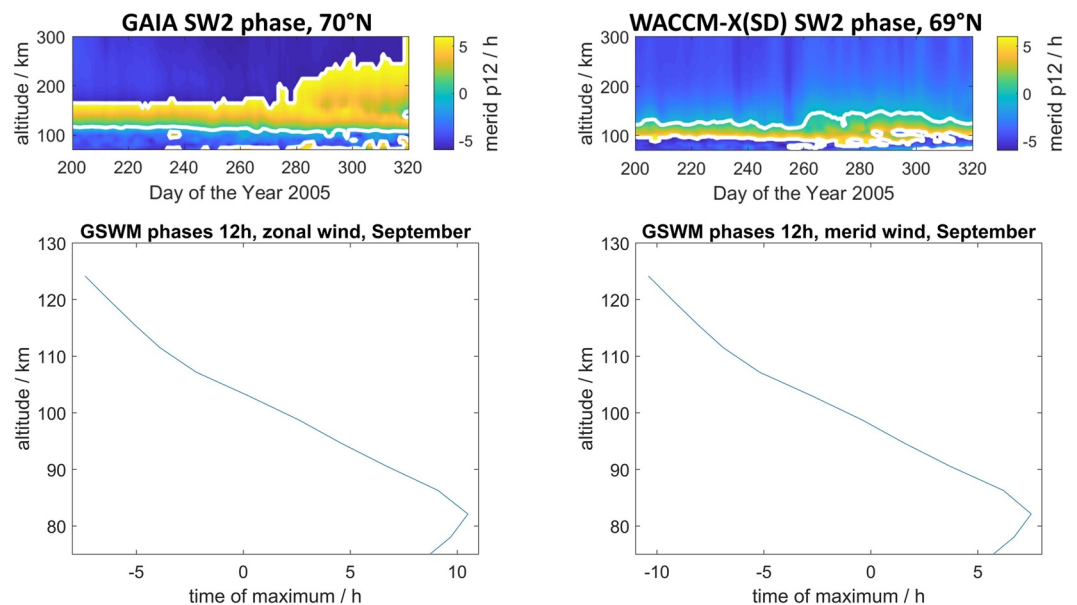


Figure 10. Top: Phases of the SW2 tidal mode in GAIA (left) and WACCM-X(SD) (right) at high-latitudes. Bottom: Phases of the 12 hr tide in zonal (left) and meridional (right) winds from GSWM at 69°N in September.

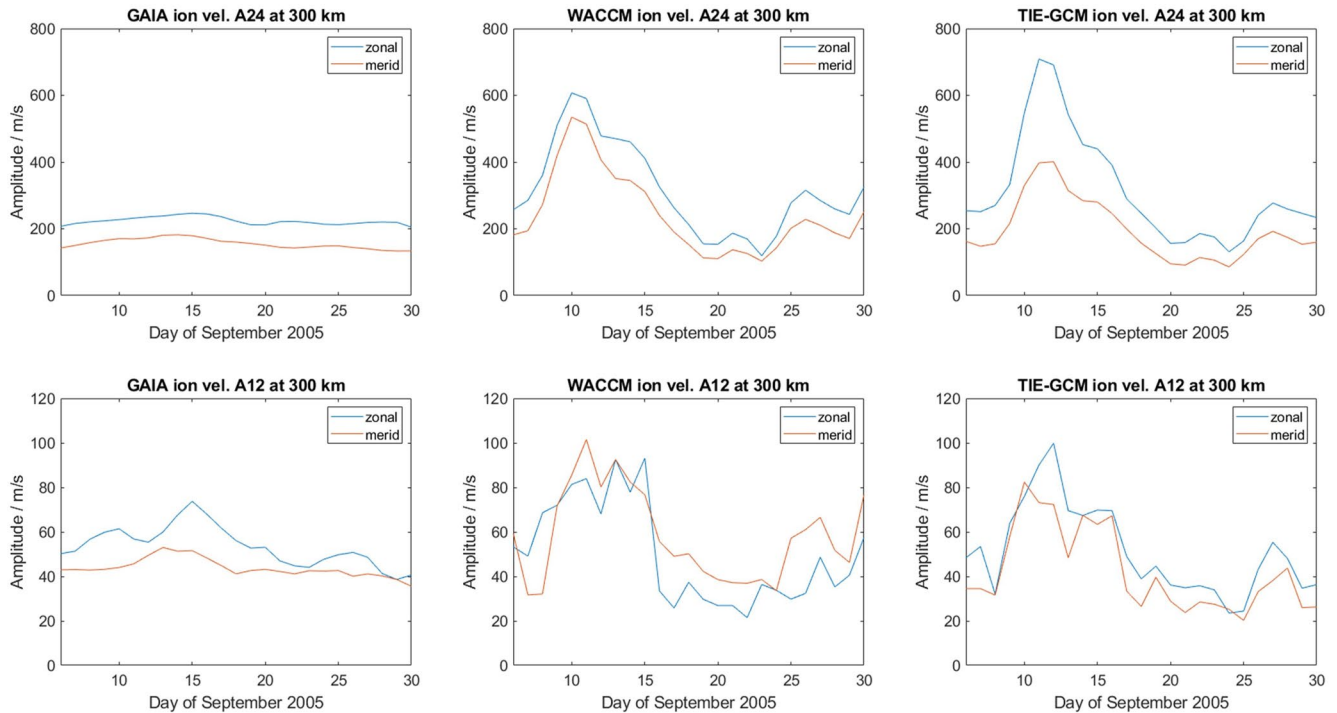


Figure 11. Diurnal (top) and semidiurnal (bottom) high altitude ion velocity amplitudes from GAIA, WACCM-X(SD), and TIE-GCM (left to right).

that asymptotes to constant phase as well as an evanescent tidal mode. This can be partly studied with the GSWM, since it does not include any in situ forcing. Consequently the GSWM phases show a steady phase progression similar to what is found at $\lesssim 120$ km in measurements (see Figure 4). A slight deceleration of the phase progression can be seen at the highest GSWM altitudes (approximately 124 km) but no rapid transition as it has been found in Figure 4. This indicates that the phase transition found in measurements and models is caused by in situ forcing. However, it should be noted that GSWM phase gradients have been found to deviate notably from measurements at high-latitudes (Manson et al., 2002) and should therefore be considered with caution.

While the constant phase at high altitude is not a definite proof, it fits the previous conclusion that the lower SW2 band is caused by upward-propagating atmospheric tides and the upper SW2 band is in situ forced. Whether propagating and evanescent tidal modes are completely separated by altitude or overlap and interfere cannot be determined definitely. However, the sudden transition around equinox (DOY 265) that is visible in the phases, especially from GAIA data at high-latitudes, could be caused by interference of several tidal modes. Since it is known that atmospheric SW2 tides undergo a transition at that time of year (Pedatella et al., 2021), the interference of atmospheric and in situ tidal oscillations might be responsible for the observed autumn transition at high altitudes. Different in situ forced tidal modes cannot be separated from looking at the phases and the interaction of tidal modes can only be presumed. However, phase progression analysis is a helpful technique to quantify the respective influence of geomagnetic and atmospheric forces and to identify the altitude where the dominant processes change.

5.3. High Altitude ion Velocities

To see whether the polar plasma convection in the models also shows a relevant 12 hr oscillation component (as did the EISCAT measurements, see Section 4.3), the oscillation amplitudes of ion velocities at approximately 300 km altitude are calculated. Considering that GAIA uses a constant cross-polar potential, it is expected that plasma convection ion velocities should indicate increased discrepancies compared to the ISR observations. WACCM-X(SD) and TIE-GCM include the K_p index to parametrize geomagnetic activity and the general trend of ion velocity oscillations should therefore resemble the measurements in Figure 5. Figure 11 shows diurnal and semidiurnal oscillation amplitudes of the ion velocity at 300 km altitude from GAIA, WACCM-X(SD), and TIE-GCM.

It can be seen that the diurnal oscillation amplitudes are dominant and show a similar trend in TIE-GCM and WACCM-X(SD) which also resembles the trend found in the measurements. Semidiurnal oscillations also have significant amplitudes and tentatively also correlate with geomagnetic activity. It can be concluded that semidiurnal oscillations at high altitudes are forced by the same plasma convection as diurnal oscillations. GAIA ion velocity amplitudes are similar to WACCM-X(SD) and TIE-GCM amplitudes at low activity times and show little variability. The ion velocity oscillations of WACCM-X(SD) and TIE-GCM are highly similar in amplitudes and dynamics.

6. Summary

Oscillation amplitudes in ISR and meteor radar neutral wind measurements showed a distinctly different behavior in zonal and meridional direction. While the ratio of 12–24 hr oscillation amplitudes in zonal neutral winds fits well into the classical expectations, meridional neutral wind show a more complex structure. Meridional wind measurements showed a region of strong semidiurnal oscillations at $\gtrsim 130$ km additionally to the expected large 12 hr amplitudes at $\lesssim 110$ km. To determine the origin of these high altitude semidiurnal oscillations, runs from three ionosphere GCMs have been analyzed.

All three models also showed a multi-band structure with strong 12 hr oscillations at high altitudes in the meridional neutral wind component. The asymmetry between zonal and meridional component was also found in all model runs. There were distinct differences between the models regarding dynamics and structure of the high altitude semidiurnal oscillations, presumably caused by different parametrizations of atmospheric, geomagnetic and solar inputs. However, interpretation of the obtained results is possible to some extent.

Comparison at different latitudes showed that the high altitude SW2 amplitudes are forced by a high-latitude effect. Tidal phases obtained from measurement and model data suggested these oscillations to be in situ forced rather than propagating upward from the middle atmosphere. Separate TIE-GCM runs with and without atmospheric tidal input to the ionosphere confirmed this by showing that while the lower SW2 band depends on the atmospheric input, the upper SW2 band remained unaffected by it. An additional TIE-GCM run with fixed low solar irradiance showed that EUV absorption clearly contributes to forcing of 12 hr oscillations at high altitudes.

However, even for constant low EUV absorption, there are high altitude SW2 oscillations which show considerable variability. Also, notably strong 12 hr oscillation amplitudes have been found in the ion velocities at approximately 300 km altitude in both measurements and models. This indicates a strong impact of polar plasma convection on semidiurnal tidal oscillations in the high-latitude thermosphere. In situ forcing of tidal oscillations in the high-latitude ionosphere at high altitudes seems to be the most likely interpretation for the obtained model and measurement results. It seems that both EUV absorption and ion convection contribute significantly to the tidal oscillation amplitudes. Whether one mechanism is dominant could not be finally determined.

7. Conclusions

It has been shown that it is possible to perform combined observations of neutral wind velocities with meteor radars and incoherent scatter radars. Such simultaneous observations are of major importance when studying the coupling of atmospheric phenomena into the ionosphere. Another methodological improvement in this paper is the first use of the ASF technique on EISCAT measurements. This technique permits to resolve the day-to-day variability of unevenly sampled time series and an improved handling of the measurement uncertainties which are highly relevant in the incoherent scatter process. This allowed to investigate a larger altitude range which revealed a previously not reported two band structure of strong semidiurnal oscillations in meridional neutral winds. Tidal oscillations at higher altitudes are presumably in situ forced. Both polar plasma convection and EUV absorption are shown to be strong forcing mechanism at high-latitudes. However, propagating atmospheric tides might play an important role as well under specific conditions. The interference of several tidal modes from different origins might then result in the observed complex vertical structuring of tidal oscillations.

Future work should target a more detailed investigation of different in situ forcing mechanisms. The latitudinal propagation of in situ forced tidal modes could give insight on the forcing mechanism. Ideally, the tidal modes forced by plasma convection and EUV absorption can be separated and their interaction studied. This would require more long-time ISR measurement campaigns as they might become possible with the upcoming EISCAT

3D system. As for modeling, plasma convection models need to be investigated and compared with respect to the size and shape of the convection pattern.

Data Availability Statement

The model and measurement data used in this paper as well as the input files for the conducted TIE-GCM runs can be found under <https://doi.org/10.5281/zenodo.6817130> (Günzkofer et al., 2022a). The data analysis and plotting software in the version used for this publication (Version 1) can be found under <https://doi.org/10.5281/zenodo.7072141> (Günzkofer et al., 2022b). All files are available under the Creative Commons Attribution 4.0 International license. In case of further questions about the data or the analysis software please contact the corresponding author.

Acknowledgments

The authors would like to acknowledge the following data sources: EISCAT is an international association supported by research organizations in China (CRIRP), Finland (SA), Japan (NIPR and ISEE), Norway (NFR), Sweden (VR), and the United Kingdom (UKRI). For this study, a data set from the Ground-to-topside model of Atmosphere and Ionosphere for Aeronomy (GAIA) project carried out by the National Institute of Information and Communications Technology (NICT), Kyushu University, and Seikei University was used. The WACCM-X model has been developed at NCAR (see <https://www2.hao.ucar.edu/modeling/wacm-x>). The TIEGCM and related Thermosphere-Ionosphere models have been developed by the “Atmosphere Ionosphere Magnetosphere” (AIM) Section of the High Altitude Observatory (HAO) at NCAR (see <https://www.hao.ucar.edu/modeling/tgcm/>). The TIEGCM data was generated on the “Kratos” High-Performance Data Analysis Cluster (HPDA). The GSWM data has been obtained from the HAO UCAR website <https://www2.hao.ucar.edu/gswm-global-scale-wave-model>. H. Liu acknowledges support from JSPS KAKENHI grants 18H01270, 17KK0095, 20H00197, and JRP-LEAD with DFG (JPJSJPR 20181602). G. Stober is a member of the Oeschger Center for Climate Change Research. Open Access funding enabled and organized by Projekt DEAL.

References

- Andrews, D. G., Holton, J. R., & Leovy, C. B. (1987). *Middle atmosphere dynamics* (Vol. 40). Academic Press.
- Barracough, D. R. (1988). IAGA division I working group 1: International geomagnetic reference field revision 1987. *Geophysical Journal International*, 93(1), 187–189. <https://doi.org/10.1111/j.1365-246X.1988.tb01397.x>
- Baumgarten, K., & Stober, G. (2019). On the evaluation of the phase relation between temperature and wind tides based on ground-based measurements and reanalysis data in the middle atmosphere. *Annales Geophysicae*, 37(4), 581–602. <https://doi.org/10.5194/angeo-37-581-2019>
Retrieved from <https://angeo.copernicus.org/articles/37/581/2019/>
- Brekke, A., Doupinik, J. R., & Banks, P. M. (1973). A preliminary study of the neutral wind in the auroral E region. *Journal of Geophysical Research*, 78(34), 8235–8250. <https://doi.org/10.1029/JA078i034p08235>
- Chapman, S. (1956). The electrical conductivity of the ionosphere: A review. *Il Nuovo Cimento - B*, 4(S4), 1385–1412. <https://doi.org/10.1007/BF02746310>
- Collis, P. N. (1995). EISCAT data base for ionospheric modelling: F-region and topside ionosphere. *Advances in Space Research*, 16(1), 37–46. [https://doi.org/10.1016/0273-1177\(95\)00096-W](https://doi.org/10.1016/0273-1177(95)00096-W)
- Folkestad, K., Hagfors, T., & Westerlund, S. (1983). EISCAT: An updated description of technical characteristics and operational capabilities. *Radio Science*, 18(6), 867–879. <https://doi.org/10.1029/RS018i006p00867>
- Gasparini, F., Liu, H., & McInerney, J. (2020). Preliminary evidence of Madden-Julian oscillation effects on ultrafast tropical waves in the thermosphere. *Journal of Geophysical Research*, 125(5), e27649. <https://doi.org/10.1029/2019JA027649>
- Gelaro, R., McCarty, W., Suárez, M. J., Todling, R., Molod, A., Takacs, L., et al. (2017). The modern-era retrospective analysis for research and applications, version 2 (MERRA-2). *Journal of Climate*, 30(14), 5419–5454. <https://doi.org/10.1175/JCLI-D-16-0758.1>
- Grassmann, V. (1993). An incoherent scatter experiment for the measurement of particle collisions. *Journal of Atmospheric and Terrestrial Physics*, 55(4–5), 573–576. [https://doi.org/10.1016/0021-9169\(93\)90006-K](https://doi.org/10.1016/0021-9169(93)90006-K)
- Günzkofer, F., Pokhotelov, D., Stober, G., Liu, H., Liu, H., Mitchell, N., et al. (2022a). [Dataset] Determining the origin of tidal oscillations in the ionospheric transition region with EISCAT radar and global simulation data. Zenodo. <https://doi.org/10.5281/zenodo.6817130>
- Günzkofer, F., Pokhotelov, D., Stober, G., Liu, H., Liu, H., Mitchell, N., et al. (2022b). [Software] Determining the origin of tidal oscillations in the ionospheric transition region with EISCAT radar and global simulation data. Zenodo. <https://doi.org/10.5281/zenodo.7072141>
- Hagan, M. E., & Forbes, J. M. (2002). Migrating and nonmigrating diurnal tides in the middle and upper atmosphere excited by tropospheric latent heat release. *Journal of Geophysical Research: Atmospheres*, 107(D24), 4754. <https://doi.org/10.1029/2001JD001236>
- Hagan, M. E., & Forbes, J. M. (2003). Migrating and nonmigrating semidiurnal tides in the upper atmosphere excited by tropospheric latent heat release. *Journal of Geophysical Research: Space Physics*, 108(A2), 1062. <https://doi.org/10.1029/2002JA009466>
- Hedin, A. E. (1991). Extension of the MSIS thermosphere model into the middle and lower atmosphere. *Journal of Geophysical Research*, 96(A2), 1159–1172. <https://doi.org/10.1029/90JA02125>
- Heelis, R. A., Lowell, J. K., & Spiro, R. W. (1982). A model of the high-latitude ionospheric convection pattern. *Journal of Geophysical Research*, 87(A8), 6339–6345. <https://doi.org/10.1029/JA087iA08p06339>
- Hocking, W. K., Fuller, B., & Vandeppeer, B. (2001). Real-time determination of meteor-related parameters utilizing modern digital technology. *Journal of Atmospheric and Solar-Terrestrial Physics*, 63(2–3), 155–169. [https://doi.org/10.1016/S1364-6826\(00\)00138-3](https://doi.org/10.1016/S1364-6826(00)00138-3)
- Hurrell, J. W., Holland, M. M., Gent, P. R., Ghan, S., Kay, J. E., Kushner, P. J., et al. (2013). The community earth system model: A framework for collaborative research. *Bulletin of the American Meteorological Society*, 94(9), 1339–1360. <https://doi.org/10.1175/BAMS-D-12-00121.1>
- Jin, H., Miyoshi, Y., Pancheva, D., Mukhtarov, P., Fujiwara, H., & Shinagawa, H. (2012). Response of migrating tides to the stratospheric sudden warming in 2009 and their effects on the ionosphere studied by a whole atmosphere-ionosphere model GAIA with COSMIC and TIMED/SABER observations. *Journal of Geophysical Research: Space Physics*, 117(A10), A10323. <https://doi.org/10.1029/2012JA017650>
- Kelly, M. C. (2009). *The Earth's ionosphere: Plasma physics and electrodynamics* (2nd ed.).
- Kobayashi, S., Ota, Y., Harada, Y., Ebata, A., Mori, M., Onoda, H., et al. (2015). The JRA-55 reanalysis: General specifications and basic characteristics. *Journal of the Meteorological Society of Japan*, 93(1), 5–48. <https://doi.org/10.2151/jmsj.2015-001>
- Lee, W., Kim, Y. H., Lee, C., & Wu, Q. (2018). First comparison of mesospheric winds measured with a Fabry-Perot interferometer and meteor radar at the King Sejong Station (62.2°S, 58.8°W). *Journal of Astronomy and Space Sciences*, 35, 235–242. <https://doi.org/10.5140/JASS.2018.35.4.235>
- Lindzen, R. S. (1979). Atmospheric tides. *Annual Review of Earth and Planetary Sciences*, 7, 199–225. <https://doi.org/10.1146/annurev.ea.07.050179.001215>
- Liu, H., Sun, Y.-Y., Miyoshi, Y., & Jin, H. (2017). ENSO effects on MLT diurnal tides: A 21 year reanalysis data-driven GAIA model simulation. *Journal of Geophysical Research: Space Physics*, 122(5), 5539–5549. <https://doi.org/10.1002/2017JA024011>
- Liu, H.-L., Bardeen, C. G., Foster, B. T., Lauritzen, P., Liu, J., Lu, G., et al. (2018). Development and validation of the whole atmosphere community climate model with thermosphere and ionosphere extension (WACCM-X 2.0). *Journal of Advances in Modeling Earth Systems*, 10(2), 381–402. <https://doi.org/10.1002/2017MS001232>

- Manson, A. H., Meek, C., Hagan, M., Koshyk, J., Franke, S., Fritts, D., et al. (2002). Seasonal variations of the semi-diurnal and diurnal tides in the MLT: Multi-year MF radar observations from 2Å 70Å°N, modelled tides (GSWM, CMAM). *Annales Geophysicae*, 20(5), 661–677. <https://doi.org/10.5194/angeo-20-661-2002>
- Nicolls, M. J., Bahcivan, H., Häggström, I., & Rietveld, M. (2014). Direct measurement of lower thermospheric neutral density using multifrequency incoherent scattering. *Geophysical Research Letters*, 41(23), 8147–8154. <https://doi.org/10.1002/2014GL062204>
- Nozawa, S., & Brekke, A. (1999). Studies of the auroral E region neutral wind through a solar cycle: Quiet days. *Journal of Geophysical Research*, 104(A1), 45–66. <https://doi.org/10.1029/1998JA900013>
- Nozawa, S., Ogawa, Y., Oyama, S., Fujiwara, H., Tsuda, T., Brekke, A., et al. (2010). Tidal waves in the polar lower thermosphere observed using the EISCAT long run data set obtained in September 2005. *Journal of Geophysical Research: Space Physics*, 115(A8), A08312. <https://doi.org/10.1029/2009JA015237>
- Nygrén, T., Aikio, A. T., Kuula, R., & Voiculescu, M. (2011). Electric fields and neutral winds from monostatic incoherent scatter measurements by means of stochastic inversion. *Journal of Geophysical Research: Space Physics*, 116(A5), A05305. <https://doi.org/10.1029/2010JA016347>
- Oberheide, J., Forbes, J. M., Zhang, X., & Bruinsma, S. L. (2011). Climatology of upward propagating diurnal and semidiurnal tides in the thermosphere. *Journal of Geophysical Research: Space Physics*, 116(A11), A11306. <https://doi.org/10.1029/2011JA016784>
- Onogi, K., Tsutsui, J., Koide, H., Sakamoto, M., Kobayashi, S., Hatsushika, H., et al. (2007). The JRA-25 reanalysis. *Journal of the Meteorological Society of Japan*, 85(3), 369–432. <https://doi.org/10.2151/jmsj.85.369>
- Pedatella, N. M., Liu, H. L., Conte, J. F., Chau, J. L., Hall, C., Jacobi, C., et al. (2021). Migrating semidiurnal tide during the September equinox transition in the Northern Hemisphere. *Journal of Geophysical Research: Atmospheres*, 126(3), e33822. <https://doi.org/10.1029/2020JD033822>
- Picone, J. M., Hedin, A. E., Drob, D. P., & Aikin, A. C. (2002). NRLMSISE-00 empirical model of the atmosphere: Statistical comparisons and scientific issues. *Journal of Geophysical Research: Space Physics*, 107(A12), 1468. <https://doi.org/10.1029/2002JA009430>
- Pokhotelov, D., Becker, E., Stober, G., & Chau, J. L. (2018). Seasonal variability of atmospheric tides in the mesosphere and lower thermosphere: Meteor radar data and simulations. *Annales Geophysicae*, 36(3), 825–830. <https://doi.org/10.5194/angeo-36-825-2018>
- Qian, L., Burns, A. G., Emery, B. A., Foster, B., Lu, G., Maute, A., et al. (2014). The ncar tie-gcm: A community model of the coupled thermosphere/ionosphere system. In *Modeling the ionosphere-thermosphere system*. In *Geophysical monograph series* (Vol. 201, pp. 73–83). American Geophysical Union. <https://doi.org/10.1002/9781118704417.ch7>
- Richmond, A. D., Ridley, E. C., & Roble, R. G. (1992). A thermosphere/ionosphere general circulation model with coupled electrodynamics. *Geophysical Research Letters*, 19(6), 601–604. <https://doi.org/10.1029/92GL00401>
- Rienecker, M. M., Suarez, M. J., Gelaro, R., Todling, R., Bacmeister, J., Liu, E., et al. (2011). MERRA: NASA's modern-era retrospective analysis for research and applications. *Journal of Climate*, 24(14), 3624–3648. <https://doi.org/10.1175/JCLI-D-11-00015.1>
- Rino, C. L., Brekke, A., & Baron, M. J. (1977). High-resolution auroral zone E region neutral wind and current measurements by incoherent scatter radar. *Journal of Geophysical Research*, 82(16), 2295–2304. <https://doi.org/10.1029/JA082i016p02295>
- Schunk, R., & Nagy, A. (2009). *Ionospheres: Physics, plasma physics, and chemistry* (2nd ed.). Cambridge University Press. <https://doi.org/10.1017/CBO9780511635342>
- Schunk, R., & Walker, J. C. G. (1973). Theoretical ion densities in the lower ionosphere. *Planetary and Space Science*, 21(11), 1875–1896. [https://doi.org/10.1016/0032-0633\(73\)90118-9](https://doi.org/10.1016/0032-0633(73)90118-9)
- Smith, A. K. (2012). Global dynamics of the MLT. *Surveys in Geophysics*, 33(6), 1177–1230. <https://doi.org/10.1007/s10712-012-9196-9>
- Stober, G., Baumgarten, K., McCormack, J. P., Brown, P., & Czarniecki, J. (2020). Comparative study between ground-based observations and NAVGEM-HA analysis data in the mesosphere and lower thermosphere region. *Atmospheric Chemistry and Physics*, 20(20), 11979–12010. <https://doi.org/10.5194/acp-20-11979-2020>
- Stober, G., Kuchar, A., Pokhotelov, D., Liu, H., Liu, H.-L., Schmidt, H., et al. (2021). Interhemispheric differences of mesosphere-lower thermosphere winds and tides investigated from three whole-atmosphere models and meteor radar observations. *Atmospheric Chemistry and Physics*, 21(18), 13855–13902. <https://doi.org/10.5194/acp-21-13855-2021>
- Stober, G., Matthias, V., Jacobi, C., Wilhelm, S., Höffner, J., & Chau, J. L. (2017). Exceptionally strong summer-like zonal wind reversal in the upper mesosphere during winter 2015/16. *Annales Geophysicae*, 35(3), 711–720. <https://doi.org/10.5194/angeo-35-711-2017>
- Straus, J. M., Creekmore, S. P., Harris, R. M., Ching, B. K., & Chiu, Y. T. (1975). A global model for thermospheric dynamics - II. Wind, density, and temperature fields generated by EUV heating. *Journal of Atmospheric and Terrestrial Physics*, 37, 1245–1253. [https://doi.org/10.1016/0021-9169\(75\)90033-1](https://doi.org/10.1016/0021-9169(75)90033-1)
- Truskowski, A. O., Forbes, J. M., Zhang, X., & Palo, S. E. (2014). New perspectives on thermosphere tides: 1. Lower thermosphere spectra and seasonal-latitude structures. *Earth Planets and Space*, 66, 136. <https://doi.org/10.1186/s40623-014-0136-4>
- Williams, P. J. S., & Virdi, T. S. (1989). EISCAT observations of tidal modes in the lower thermosphere. *Journal of Atmospheric and Terrestrial Physics*, 51(7), 569–577. [https://doi.org/10.1016/0021-9169\(89\)90055-X](https://doi.org/10.1016/0021-9169(89)90055-X)
- Wu, Q., Jee, G., Lee, C., Kim, J.-H., Kim, Y. H., Ward, W., & Varney, R. H. (2017). First simultaneous multistation observations of the polar cap thermospheric winds. *Journal of Geophysical Research: Space Physics*, 122(1), 907–915. <https://doi.org/10.1002/2016JA023560>